ARTICLE

Nanostructured terbium-doped ceria spheres: Effect of dopant on physical and chemical properties under reducing and oxidizing conditions

L. M. Acuña,[a,b] F. F. Muñoz,[a,b] C. A. Albornoz,[c] A. G. Leyva,[c,d] R. T. Baker[e] and R. O. Fuentes[b,c],

In this work, nanostructured $Ce_{1-x}Tb_xO_{2-\delta}$ (x = 0.1 and 0.2) spheres were synthesized by microwave assisted hydrothermal homogeneous co-precipitation and their properties were characterized by synchrotron radiation X-ray diffraction (XRD), X-ray absorption spectroscopy (XAS) and scanning and high resolution electron microscopy (SEM and HRTEM) with energy dispersive X-ray spectroscopy (EDS). Spherical particles with average diameters around 200 nm were obtained in excellent yields. In order to compare the effect of the morphology on the physico-chemical properties, terbium-doped ceria nanopowders were also synthesized by a cation complexation method. *In situ* XRD, X-ray absorption near-edge spectroscopy (XANES) and extended X-ray absorption fine structure (EXAFS) experiments were carried out under reducing and oxidizing conditions in order to investigate the redox behaviour of these materials and to evaluate the oxidation state ratios in the Ce^{3+}/Ce^{4+} and Tb^{3+}/Tb^{4+} couples. All of the $Ce_{1-x}Tb_xO_{2-\delta}$ samples were found to have a cubic crystal structure (Fm-3m space group). The spheres were composed of nanoparticles with an average crystallite size of about 10 nm. *In situ* XRD experiments showed an increase in lattice parameters on reduction which was attributed to the reduction of Ce^{4+} and Tb^{4+} cations to Ce^{3+} and Tb^{3+}, which have larger radii, and to the associated increase in V_O concentration. The effect of synthesis method on structural properties was evident in that the percentage of Tb present as Tb^{3+} in the nanostructured spheres was larger than in the nanopowders of the same elemental composition.

Introduction

Applications such as three-way catalysts, oxygen gas sensors and electrodes and electrolytes for solid oxide fuel cells mean that ceria-based mixed oxides are materials with a large technological impact, especially in the area of environmental protection.[4] Many of these applications rely on the high oxygen ion conductivity and oxygen storage capacity which can easily be achieved in ceria by doping with other aliovalent cations, such as rare earth elements (e.g. Gd, Pr, Tb). This creates oxygen vacancies which enable migration of oxygen ions through the lattice.[6] The oxygen ion vacancies ($V_O^{\bullet\bullet}$) are responsible for the ionic conductivity of the doped ceria.[7,8] Because they exhibit high ionic conductivity at moderate temperatures (above 600°C), these materials are considered promising for application in electrolytes for intermediate temperature solid oxide fuel cells (IT-SOFCs).[9,10] However, oxygen ion vacancies can also be created by interaction of the

ceria with the gas-phase. Under reducing atmospheres, both electronic (Ce'_{Ce}) and ionic ($V_O^{\bullet\bullet}$) charge carriers can be created through loss of oxygen ions from the lattice as molecular oxygen. The presence of both ionic and electronic charge carriers gives rise to mixed (ionic and electronic) conducting behaviour in both undoped and doped cerias (e.g. Lanthanide-doped cerias, LnDCs) under reducing conditions. This is a difficulty for the application of LnDCs in SOFC electrolytes – where electronic conductivity would give rise to an internal short circuit of the electrolyte - but would be an advantage for the use of these doped cerias in anodes for IT-SOFCs. This and the increasingly wide use of such materials as catalyst components has prompted a renewed interest in their preparation in the form of nanostructured materials with controlled morphologies and high surface areas.[11]
Ceria doped with a univalent cation - for example, gadolinia-doped ceria - shows n-type electronic conductivity due to the partial reduction of Ce^{4+} to Ce^{3+} at high temperatures (>600ºC)

under reducing conditions.[12] However, ceria doped with a multivalent cation (e.g. M^{3+}/M^{4+}) can exhibit mixed (n type and oxygen ion) conduction at higher oxygen partial pressures, because of the stability of the lower oxidation state of the dopant ion (M^{3+}). This enables the application of these materials in oxygen separation membranes.[13,14] It has been reported that the presence of multivalent praseodymium ($Pr^{3+,4+}$) in Pr-doped ceria enhanced the formation and migration of oxygen vacancies and that, on reduction of the oxide – creating oxygen ion vacancies – the formation of Pr^{3+} was favored over the formation of Ce^{3+}.[15-17]

Recently, the authors reported on nanostructured Gd- and Pr-doped ceria (GDC and PrDC respectively) spheres, obtained by a microwave-assisted hydrothermal homogeneous co-precipitation technique.[18] In that work, *in situ* XRD experiments showed an increase in lattice parameter on reduction which was attributed to the reduction of Ce^{4+} and Pr^{4+}cations to Ce^{3+} and Pr^{3+}, which have larger radii, and to the associated increase in V_O concentration. This increase in lattice parameter was much more pronounced for PrDC than GDC, and was explained by the much larger change in ionic radius for Pr on reduction. XANES absorption experiments at the Ce and Pr L_3-edges showed that the changes observed on reduction of the Pr-containing samples resulted mostly from the formation of Pr^{3+} rather than Ce^{3+}, and supported the previously-reported proposal that Pr^{3+} acts to stabilize Ce^{4+} to some extent.[18]

In the present work, we report the redox properties of ceria materials doped with multivalent Tb cations ($Tb^{3+,4+}$) and possessing a controlled morphology. Nanostructured $Ce_{0.9}Tb_{0.1}O_{2-\delta}$ and $Ce_{0.8}Tb_{0.2}O_{2-\delta}$ spheres were synthesized by a microwave-assisted hydrothermal homogeneous co-precipitation technique. In order to compare the effect of the morphology on the physico-chemical properties, terbium-doped ceria nanopowders of the same chemical compositions were also synthesized by a cation complexation method. The resulting samples were characterized by synchrotron radiation X-ray diffraction (SR-XRD), X-ray absorption near-edge spectroscopy (XANES), extended X-ray absorption fine structure (EXAFS), scanning and high resolution transmission electron microscopy (SEM and HRTEM) and energy dispersive X-ray spectroscopy (EDS). The redox properties of the materials were studied using *in situ* XAS (XANES and EXAFS) and XRD experiments carried out under reducing and oxidizing atmospheres at temperatures up to 500 ºC.

Experimental

Nanostructured $Ce_{0.9}Tb_{0.1}O_{2-\delta}$ (TbDC10) and $Ce_{0.8}Tb_{0.2}O_{2-\delta}$ (TbDC20) spheres were synthesized by a microwave-assisted hydrothermal homogeneous co-precipitation technique (HMW).[18] $Ce(NO_3)_3.6H_2O$ (99.99%, Alfa Aesar) and $Tb(NO_3)_3.6H_2O$ (99.9%, Alfa Aesar) were employed as precursors. Each nitrate was dissolved in pure deionized H_2O separately and then the solutions were mixed to obtain a 0.1 M nitrate solution with molar ratios of Ce:Tb appropriate for the preparation of TbDC10 and TbDC20, respectively. Urea was added in order to give a molar ratio of urea:final of 4:1 and 60 ml of the resulting solution was placed in a Teflon-lined autoclave. A Milestone ETHOS 1 Advanced Microwave Digestion system was employed. The sealed autoclave was placed in the oven and was heated to 120ºC with a ramp rate of 30ºC.min^{-1}- with oven power set to 550 W - and then kept at this temperature for 1 h. After cooling, the white powder product was collected by centrifugation (2.5 min at 7830 rpm)

and dried at 37ºC for 12 h. After calcination at 500ºC in air for 1 h, the nanostructured TbDC spheres were obtained.

In order to compare the physico-chemical properties of the spheres with those of a simple powder, terbium-doped ceria nanopowders of the same two compositions were synthesized by the cation complexation method (CC) previously reported by the authors to obtain GDC.[9] $Ce(NO_3)_3.6H_2O$ (99.99%, Alfa Aesar) and $Tb(NO_3)_3.6H_2O$ (99.9%, Alfa Aesar) were employed as precursors. Each nitrate was dissolved in d.i. H_2O separately and then the solutions were mixed to obtain nitrate solutions with molar ratios of Ce:Tb appropriate for the preparation of products with the same compositions as the TbDC10 and TbDC20 samples. Citric acid (99.5%, Merck) was dissolved in d.i. water and this was added to the cation nitrate solution in appropriate amounts to give a molar ratio of final total oxide (TO) to citric acid (CA) of 1:2. After homogenization of this solution, the temperature was raised to 80°C, and the solution maintained under stirring to remove excess water and to convert it to a transparent gel. While raising the temperature, the solution became more viscous with evolution of foam, and finally it gelled without any visible precipitation or turbidity. During the dwell at 80°C there was an increase in viscosity and simultaneous elimination of water and NO_2. The initial thermal decomposition of the precursor was carried out at 250°C for 1 h in air and the resulting ash-like material was calcined at 500°C for 1 h in air.

In order to verify the phase composition, conventional X-ray diffraction (XRD) was performed in a PANalytical Empyream2 with a PIXcell^{3D} detector employing Cu-K_α radiation (of wavelength 1.5418 Å). Data in the angular range $2\theta = 20 - 90°$ were collected in step-scanning mode, with a step length of 0.04° and a step-counting time of 4 s. The average crystallite size, D_{XRD}, of the products was determined using the Scherrer formula[19] from the extent of peak broadening of the main XRD reflection (111). Errors in crystallite size were derived by estimating the error in the FWHM (full-width at half-maximum) to be equal to the 2θ step.

Nitrogen adsorption-desorption isotherms were obtained using an Autosorb-1 instrument from Quantachrome. Outgassing was carried out at 200ºC for 16 h prior to the measurements. Analysis of the isotherms using the BET method provided values of the specific surface area (SSA) of the samples.

SEM images were obtained in secondary electron mode using a JEOL 6700F instrument with Field Emission Gun (FEG). A JEOL JSM 5600 instrument equipped with an EDS spectrometer was used to record EDS spectra. Values of accelerating voltage (in kV) and working distance (WD) are provided in the images. For imaging in the FEG-SEM, samples were gold-coated. The image analysis software, Scion Image, was used to obtain particle size information from the SEM images.

TEM images were obtained using a JEOL JEM 2011 instrument operating with a LaB_6 filament at an accelerating voltage of 200 kV and equipped with an Oxford Instruments EDS spectrometer. The images were captured using a Gatan CCD camera and analyzed using Digital Micrograph 3.4.4 software. The TEM microscope was also used to obtain EDS spectra and to record two-dimensional elemental distribution maps. For TEM examination the samples were suspended in acetone using ultrasonication and deposited onto holey carbon-coated Cu grids.

XRD patterns were recorded at high temperatures (HT) and in controlled atmospheres using synchrotron radiation at the D10B-XPD beamline of the National Synchrotron Light

Laboratory (LNLS, Campinas, Brazil). In these *in situ* XRD experiments, the sample was mounted on a ceramic sample-holder and placed in a furnace. The X-ray wavelength was set at 1.54892 Å. Data in the angular range $2\theta = 20 - 100°$ were collected in step-scanning mode, with a step length of 0.04° and a step-counting time of 2 s. The data were collected at temperatures ranging from room temperature to 500°C. The sample was heated at a rate of 10°C/min, and a soak time of 10 min was employed at each temperature step before performing the XRD scan. The thermal and redox behavior of the materials was studied in 5% H_2/He (total flow: 20 ml.min^{-1}) and in dry synthetic air (total flow: 50 ml.min^{-1}). NIST SRM 640c Si powder was used as the standard for the instrumental broadening correction.

In situ XAS (XANES) experiments under conditions of controlled temperature and atmosphere were carried out at the D04B-XAFS1 beamline at LNLS in transmission mode using a Si(111) monochromator for the Ce L$_3$-edge (5726 eV) and Tb L$_3$-edge (7515 eV). The nominal photon flux of the beamline is 3×10^9 photons/(s.mrad.100mA)@6keV. All spectra were collected at energies in the range 5690-6100eV (for the Ce L$_3$-edge) and 7480-8200eV (for the Ce L$_3$-edge) with E/ΔE=5000 to 10000 in both cases. Energies for the Ce L$_3$-edge and Tb L$_3$-edge were calibrated using a Cr foil (5989 eV) and Co foil (7709 eV), respectively. Two acquisitions were made on the same sample to improve the signal to noise ratio. Samples were diluted with boron nitride and these mixtures were pressed into 15 mm diameter pellets (around 6 mg of sample and 70 mg of diluent were used). For the transmission measurements, the pellets were placed in a tubular quartz furnace (diameter, 20 mm; X-ray path length, 440 mm) sealed with refrigerated Kapton windows. Temperature was measured and controlled by a thermocouple passed down the sample holder and positioned close to the surface of the pellet. Temperature-resolved XAS spectra at the Ce L$_3$-edge and Tb L$_3$-edge were acquired during temperature programmed reduction (TPR) under 5% H_2/He (total flow: 20 ml.min^{-1}) at temperatures from 25 to 500°C at a heating rate of 10 °C.min^{-1} and with a total data acquisition time of 20 min per spectrum. After the data were collected at 500°C under 5% H_2/He, the system was purged with N_2 (100 ml.min^{-1}) and synthetic air (21% O_2/N_2; total flow: 50 ml.min^{-1}) was passed through the furnace. After 10 min, data were collected under these oxidizing conditions.

Results and discussion

Morphological and structural properties

In **Figure 1**, conventional X-ray diffraction (XRD) patterns are shown for the TbDC10 material in its as-synthesized form (after MW heating at 120°C for 1 h), after calcination at 250 °C for 1 h and after calcination at 500°C for 1 h. At 250°C, all of the characteristic peaks expected for TbDC10 were already observed (**Figure 1(b)**). However, these peaks are relatively broad, indicating that the average crystallite size was very small (about 4-5 nm). In **Figure 1(c)**, after calcination at 500 °C, the peaks were narrower. Even so, the crystallite sizes estimated from the peak widths were still very small (11 nm). Similar behavior was found for TbDC20, but the average crystallite sizes were slightly smaller (9 nm). In **Table 1**, average crystallite size (D$_{XRD}$), specific surface area (SSA) and the primary particle size (d$_{BET}$), calculated from the BET data, are summarized for all samples after calcination at 500°C. Of the two spherical materials, TbDC10 had the higher SSA value

(27.8 m^2.g^{-1}). The d$_{BET}$/D$_{XRD}$ ratio in TbDC20 spheres was 5.7, indicating that the crystallites exhibited a high degree of agglomeration. Similar values of primary particle size were obtained for TbDC nanopowders prepared by cation complexation although the extent of agglomeration was slightly lower than for the spherical materials.

Table 1- Average crystallite size (DXRD), specific surface area (SSA) and calculated primary particle size (dBET) for TbDC solid solutions obtained by cation complexation (CC) and microwave assisted hydrothermal homogeneous co-precipitation (HMW).

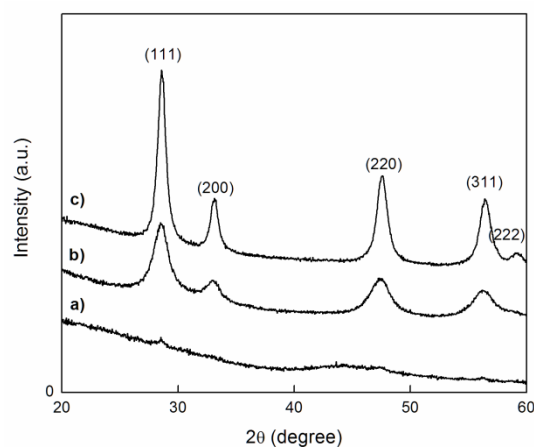| Sample	D_{XRD} / nm	SSA / m^2.g^{-1}	d_{BET} / nm	d_{BET} /D_{XRD}
TbDC10-HMW	11.1	27.8	34.6	3.1
TbDC20-HMW	9.3	18.0	53.5	5.7
TbDC10-CC	11.0	40.6	23.7	2.2
TbDC20-CC	9.3	29.3	32.9	3.5

Figure 1. XRD patterns of TbDC10 obtained by microwave assisted hydrothermal homogeneous co-precipitation (a) as-synthesized and after calcinations for (b) 1 h at 250 ºC and (c) 1 h at 500ºC.

The morphology and chemical compositions of the nanostructured TbDC spheres were studied by SEM and TEM. The microwave method gave rise to products with very high yields of spherical particles. As can be seen in the SEM images presented in **Figure 2**, there was very little extraneous material and incomplete or broken spheres –such as the one circled in **Figure 2(c)** - were very rare. The higher magnification images show the generally uniform spherical morphology of the individual particles. The diameters of large samples of particles were measured from the SEM images. Average diameters of around 200 nm were found with narrow size distributions, as shown in **Table 2**. The TbDC20 product clearly had slightly larger particles than the TbDC10 material.

Table 2- Average sphere diameter (DS), and Tb:Ce molar ratios obtained by EDS in SEM and TEM instruments together with target values, for products made using the HMW method. Ranges of ± one standard deviation are given in all cases.

Sample	D_S/ nm	molar ratio of Tb:Ce		
		SEM	TEM	target
TbDC10-HMW	188 ± 28	0.106 ± 0.006	0.135 ± 0.004	0.111
TbDC20-HMW	233 ± 30	0.269 ± 0.013	0.312 ± 0.023	0.250

The low magnification TEM images presented in **Figure 3(a)** and **(d)** confirm this small difference in particle diameter

between the two compositions as well as the narrow particle size distributions in both cases and the close-to-ideal spherical morphology of the particles in general. At intermediate magnifications (in **Figure 3(b)** and **(e)**) it is clear that the particles are essentially solid spheres comprising a large number of small particles. In the high resolution images of the sphere edges (in **Figure 3(c)** and **(f)**), these small particles are seen to be crystallites with lattice plane spacings consistent with those of ceria. These crystallites have diameters of around 10 nm but detailed analysis is not possible because of their high degree of overlap.
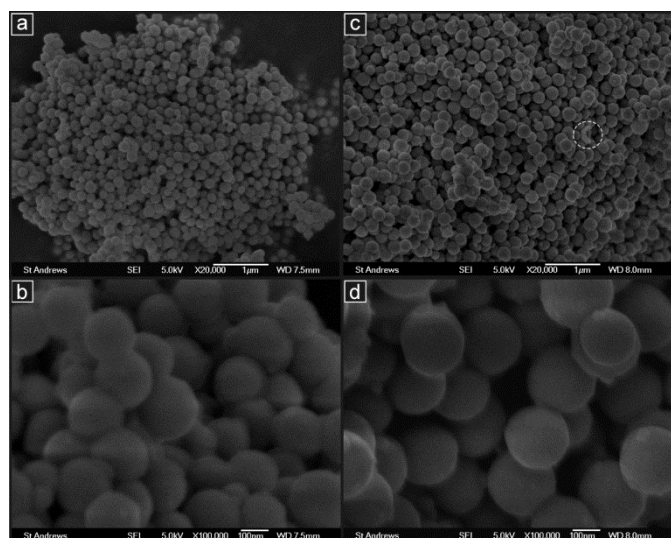
Figure 2. Medium and high magnification SEM images of (a,b) TbDC10 spheres; and (c,d) TbDC20 spheres. A very small number of broken spheres, such as that circled in (c), were observed.
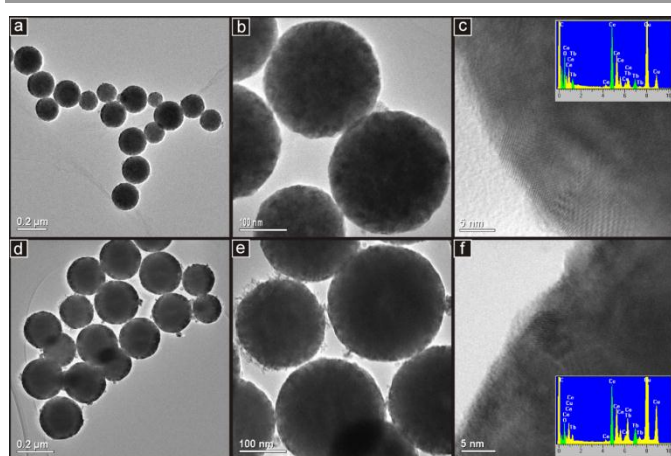

Figure 3. TEM images recorded at low, medium and high magnifications of (a,b,c) TbDC10 spheres; and (d,e,f) TbDC20 spheres. EDS spectra taken from large clusters of spherical particles of TbDC10 and TbDC20 are inset in (c) and (f), respectively (C and Cu peaks are from the TEM grid).

Table 2 presents compositional data for the two HMW samples in the form of average Tb:Ce molar ratios obtained in the SEM and the TEM. Typical EDS spectra – obtained from clusters of spheres in the TEM - are presented in **Figure 3**. The values obtained in the SEM are in good agreement with the target ratios while those recorded in the TEM are slightly higher. This

may be because the areas analyzed were smaller in the TEM than in the SEM and may be indicative of some variability in chemical composition on the sub-micron scale. Two-dimensional maps obtained using the EDS spectrometer in the TEM and showing the distribution of Ce, O and Tb across small clusters of three spheres each of TbDC10 and TbDC20 are shown in **Figure 4** together with the corresponding electron images. In both cases, the three elements can be seen to be generally coincident and their concentrations to vary in very similar ways as a function of spatial position; no segregation into Ce-rich and Tb-rich areas is evident. This indicates that the material of the spheres has at least an approximately homogeneous Ce-Tb-O composition across each sample.
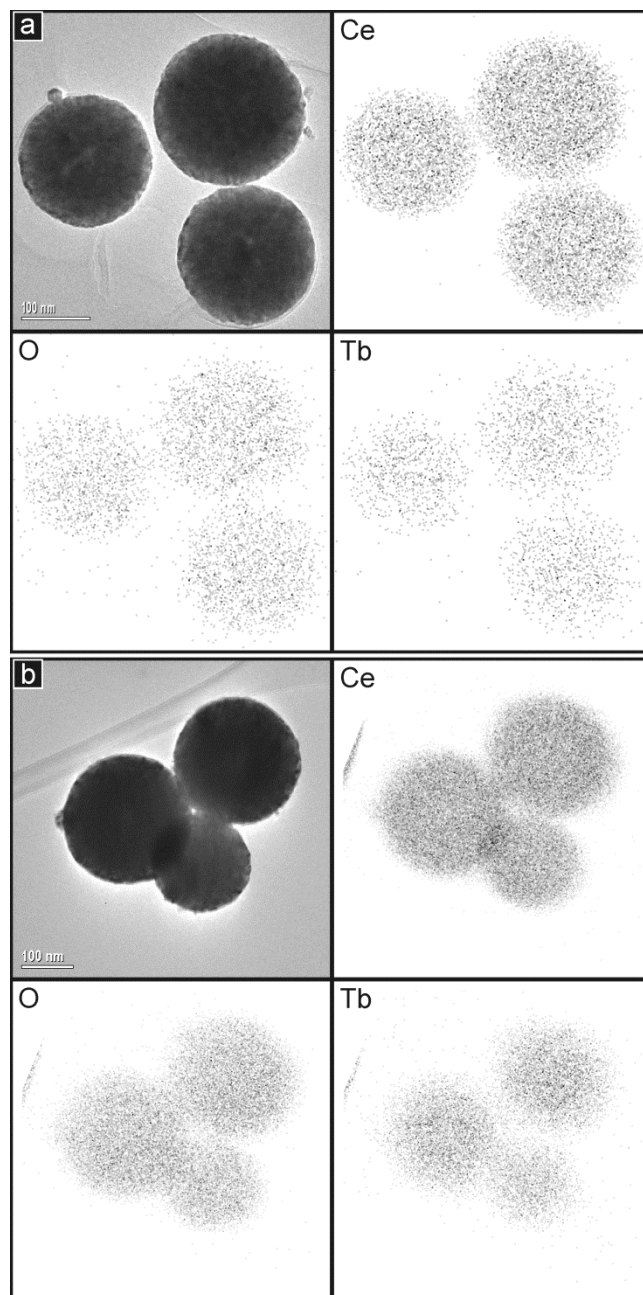

Figure 4. Electron images and EDS maps of Ce, O and Tb obtained in the TEM for small groups of (a) TbDC10 spheres; and (b) TbDC20 spheres.

Structural properties at room temperature: SR-XRD and XANES studies

A crystallographic study was performed by Rietveld refinement of the synchrotron radiation X-ray diffraction (SR-XRD) data employing the FullProf suite of software.[20] For the cubic phase, the *Fm-3m* space group was assumed, with (Tb^{4+}, Tb^{3+}, Ce^{4+}) cations and O^{2-} anions in 4a and 8c positions, respectively. The peak shape was assumed to be a pseudo-Voigt function. The background of each profile was fitted using a six-parameter polynomial function in $(2\theta)^n$, n = 0–5. The thermal parameters were assumed to be equal. SR-XRD patterns recorded at room temperature for the TbDC10 and TbDC20 samples obtained by cation complexation (CC) and microwave assisted hydrothermal homogeneous co-precipitation (HWM) are exhibited in **Figure 5(a)** and **(b)**, respectively. In the same figure, the Rietveld fitted pattern (line) and the difference plot are included.
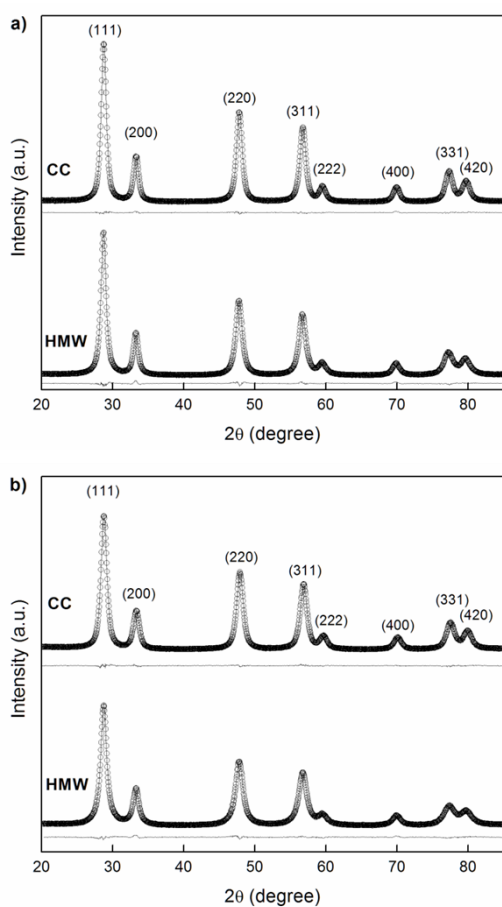

Figure 5. Synchrotron XRD patterns recorded at room temperature (empty circles) with the Rietveld-fitted pattern (line) and the difference plot for (a) TbDC10 and (b) TbDC20 obtained by cation complexation (CC) and microwave assisted hydrothermal homogeneous co-precipitation (HMW).

The results of Rietveld refinement of the SR-XRD data are summarized in **Table 3**. In this table the refinements are accompanied by reliability indices to judge the fitting quality. These indices are weighted R (R_{wp}), the reduced chi-squared (χ^2), and R_e, which are related just to the profile of the XRD patterns, and R_p, which is related to the crystal structure. The reduced chi-squared is defined as $(R_{wp}/R_e)^2$, where R_{wp} is the index that should be analyzed to verify if the refinement is converging and R_e is the expected statistical value for R_{wp}.[21] At room temperature, the lattice parameter of all the TbDC products was smaller than that for pure ceria (5.4117 Å).

Table 3. Structural parameters and standard Rietveld agreement factors for SR-XRD patterns taken at room temperature of TbDC samples obtained by cation complexation (CC) and microwave assisted hydrothermal homogeneous co-precipitation (HWM).

Sample	TbDC10-HMW	TbDC20-HMW	TbDC10-CC	TbDC20-CC
Space Group	*Fm-3m*	*Fm-3m*	*Fm-3m*	*Fm-3m*
a (Å)	5.4070(6)	5.4049(4)	5.4032(5)	5.3931(4)
V (Å^3)	158.077(3)	157.896(3)	157.750(1)	156.860(1)
R_p	3.22	3.06	2.39	2.46
R_{wp}	3.84	3.73	2.95	3.06
R_e	2.29	2.45	2.25	2.45
χ^2	2.80	2.32	1.72	1.56

In order to appreciate the difference in lattice parameters, they are plotted as a function of Tb content in **Figure 6**. It is possible to observe different slopes for TbDC obtained by cation complexation (squares) and by microwave assisted hydrothermal homogeneous co-precipitation (black circles). In the same figure, the theoretical Vegard´s slopes (dotted lines) both for total substitution by Tb^{3+} and by Tb^{4+}, in accordance with the work of Balaguer et al, are included.[15] Vegard´s law is an empirical linear relationship at constant temperature between the crystal lattice parameter and the concentration of the dopant element. Deviations from this line may indicate segregation of the dopant from the solid solution. However, single phases were observed for all samples (**Figure 5**), so, in this case, the deviation of the experimental points from the Vegard´s lines, and the fact that the points fall between the lines, is a strong indication of the presence of terbium in mixed valence (4+/3+) in the solid solution. According to this interpretation of **Figure 6**, samples obtained by cation complexation exhibited higher Tb^{4+} content than samples prepared by HMW. That is, the synthesis method seems to play an important role on the Tb^{4+}:Tb^{3+} ratio in these materials. Under the conditions relevant to the current work, both cerium and terbium can be considered to be multivalent because two oxidation states − the +3 and +4 − are accessible to each. In oxides of both metals, a mixture of +3 and +4 states can exist giving rise to non-stoichiometric phases. The ratio of the oxidation states and, therefore, this non-stoichiometry vary with the temperature and the oxygen partial pressure experienced by the material. Therefore, in mixed oxides with a specific ratio of Tb to Ce different oxygen contents are possible (while retaining the fluorite phase).[22,23] The oxygen content depends on the material preparation and subsequent treatmentand, therefore, on the synthesis method, which always includes at least an energy transfer step.[24,25] This

could explain the differences seen between materials prepared by the HMW and CC methods. In the CC method, the thermal decomposition of the precursor involves release of heat which could raise the temperature locally. This, combined with the possibility that the oxygen content of the air surrounding the sample could be significantly modified by products of combustion of the complex precursor, may give rise to a final solid with different stoichiometries, in terms of Ce^{3+}/Ce^{4+} and Tb^{3+}/Tb^{4+} ratios and oxygen content, and these may persist (to some extent) despite the final thermal treatment in the oven. In contrast, the HMW synthesis is hydrothermal and so much more controlled, and every step in the synthesis, particularly the steps involving nucleation and co-precipitation, involve more moderate conditions. Hence, the mixed oxide system is clearly capable of showing differences in the $Tb^{3+}:Tb^{4+}$ ratio, not only between samples of different Tb contents (which would be logical) but also between samples with the same Tb:Ce ratio but made by different synthesis methods. This provides a possible explanation for the lattice parameter results of **Figure 6**.
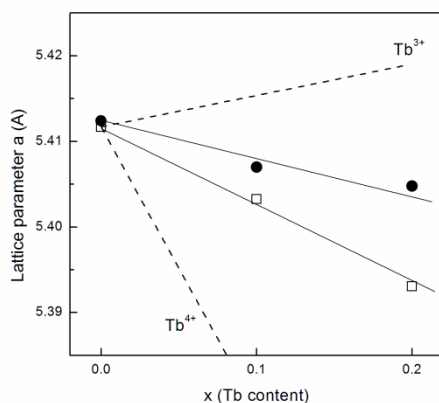

Figure 6. Lattice parameters of TbDC obtained by cation complexation (squares) and microwave assisted hydrothermal homogeneous co-precipitation (circles) as a function of Tb content. Theoretical Vegard´s slopes (dotted lines) for total substitution by Tb^{3+} and Tb^{4+} according to Balaguer et al.[15] are also plotted.

In **Figure 7(a-d)**, normalized XANES spectra obtained in air at room temperature at the Ce L_3-edge for the TbDC10-HMW, TbDC10-CC, TbDC20-HMW and TbDC20-CC samples, respectively, are presented. These exhibit two clear peaks frequently labelled A and B. Peak A is assigned as a Ce^{4+} peak with the final state $2p4f^05d^1$, which denotes that an electron is excited from the Ce 2p shell to its 5d shell, with no electron in the 4f shell. Peak B is also a Ce^{4+} peak, with the final state $2p4f^15d^1v$, which denotes that in addition to an electron excited from the Ce 2p shell to the 5d shell, another electron is also excited from the valence band (O 2p shell) to the Ce 4f shell, leaving a hole (v) in the valence band.[26] Some authors refer to Peak C as a Ce^{3+} peak.[26] An additional small peak (D) is present at pre-edge and likely arises from transitions to the bottom of the conduction band. Clearly, no large differences are observed between the spectra in **Figure 7**. The Ce L_3-absorption edges for all samples are close to 5725.7eV (values were determined from the first and second derivatives of the Ce L_3-edge XANES spectra for each sample).

In order to determine the fraction of Ce present as Ce^{3+} in the samples, data analysis was conducted by least-squares fitting four Gaussian profiles and one arctangent function to the experimental XANES data in the range between 5710 and 5750

eV. The ratio between the area of peak C (associated with Ce^{3+}) and the sum of the areas of peaks A, B and C (A and B are associated with Ce^{4+}) gives direct information about the fraction of Ce present as Ce^{3+}.[27]
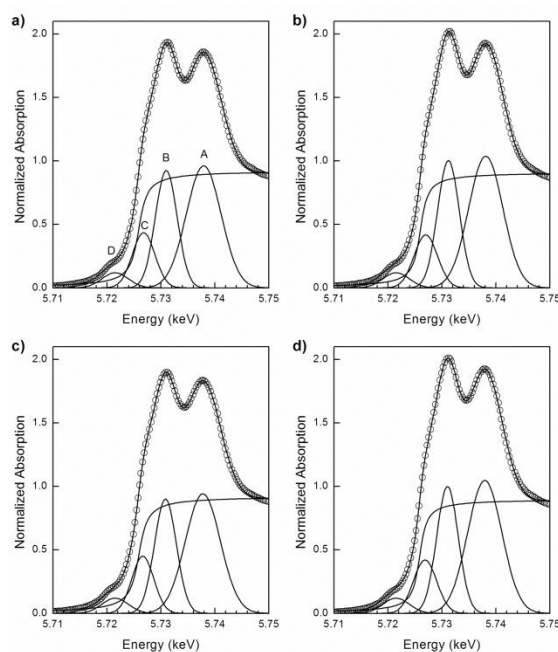

Figure 7. Normalized XANES spectra obtained at room temperature at the Ce L3-edge for (a) TbDC10-HMW and (b) TbDC10-CC, (c) TbDC20-HMW and (d) TbDC20-CC, showing the experimental data (empty circles), four Gaussian peaks (A-D), and one arctangent function obtained by least-squares fitting and the sum of all five functions (continuous black lines).

In all cases (**Table 4**), no large differences were observed in the fractions of $Ce^{3+}/(Ce^{4+}+Ce^{3+})$ in air at room temperature. In agreement with the previously proposed idea that changes in the lattice parameter are ascribed mainly to changes in the relative $Tb^{3+}:Tb^{4+}$ ratio, these results could indicate that in these samples the Ce^{4+} state is stabilized by Tb^{3+}, a proposition that will be further discussed in the following sections.

Table 4- Fraction of Ce present as Ce^{3+} in TbDC10 and TbDC20 samples at room temperature, estimated from fittings to the Ce L_3-edge XANES spectra.

Sample	$Ce^{3+}/(Ce^{4+}+Ce^{3+})^a$ (%)
TbDC10-HMW	-0.2
TbDC20-HMW	0.1
TbDC10-CC	-1.1
TbDC20-CC	-1.2

[a] Values are calculated with respect to a standard material: pure, nanoparticulate ceria. Negative values indicate that the sample contained a smaller percentage of Ce^{3+} than this standard.

The normalized XANES spectra (**Figure 8**) recorded in air at room temperature at the Tb L_3-edge clearly show the white lines corresponding to Tb^{3+} and Tb^{4+}. This indicates the presence of both Tb^{3+} and Tb^{4+} in the solid solution, supporting

the previous assumption about the lattice parameters of TbDC10 and TbDC20 obtained from analysis of the SR-XRD patterns. However, for both compositions, the $Tb^{3+}:Tb^{4+}$ ratio in the sample prepared by HMW is larger than for that prepared by CC. This is consistent with the fact that the lattice parameters were larger in the samples obtained by HMW, as was seen in **Figure 6**. This effect can be attributed exclusively to the presence of Tb^{3+}, because the Ce^{3+} content is very similar in all samples.
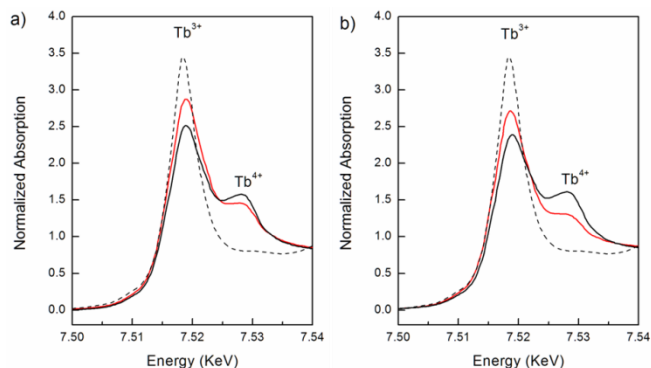

Figure 8. Normalized XANES spectra obtained at room temperature in air at the Tb L$_3$-edge for (a) TbDC10 and (b) TbDC20 obtained by cation complexation (black line) and microwave assisted hydrothermal homogeneous co-precipitation (red line). Spectra for Tb(NO$_3$)$_3$ (Tb^{3+}; dotted line) are included for comparison.

In order to investigate these effects further, SR-XRD and XANES experiments were performed on these materials *in situ* in both reducing and oxidizing environments.

In situ SR-XRD studies

In **Figure 9**, lattice parameters at 500ºC under reducing and oxidizing conditions are given. In all cases, the lattice parameters were refined assuming a cubic phase (Fm-3m space group) by the Rietveld method (see Supporting Information, Tables S1-S4). For comparison, lattice parameters corresponding to CeO$_2$ nanopowders are included in this figure.
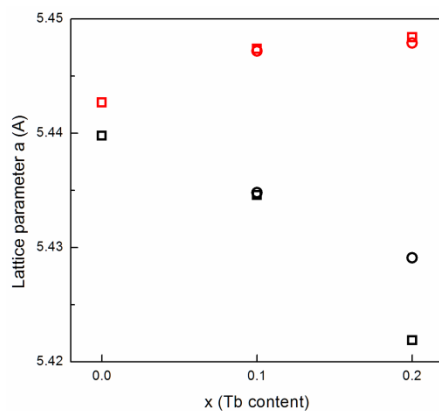

Figure 9. Lattice parameters obtained at 500ºC under reducing (red) and subsequent oxidizing (black) conditions of TbDC samples obtained by cation complexation (squares) and microwave assisted hydrothermal homogeneous co-precipitation (circles) as a function of Tb content.

When the samples were heated from room temperature to 500ºC under reducing conditions (5% H$_2$/He), the lattice parameters increased in all samples as can be seen by comparing the lattice parameters under reducing conditions at 500ºC in Figure 9 (red symbols) with those of the corresponding compositions measured at room temperature in Figure 6. This increase is due both to the thermal expansion of the unit cell and the partial reduction of Ce and Tb in the solid solutions. On switching to oxidizing conditions (synthetic air) at 500ºC, the lattice parameters were seen to decrease for all samples, but to different extents. Clearly, the unit cell parameter is strongly dependent on the concentration of the cation dopant as well as on the gas atmosphere and temperature. The difference between lattice parameters in the reducing and oxidizing conditions is small for the pure ceria, considerably larger for the two TbDC10 samples and larger again for the TbDC20 samples. In fact, for the samples prepared by the CC method, this difference doubles as the Tb content doubles (That this is not the case for the samples prepared by the HMW method may be a consequence of slower reduction kinetics caused by the more agglomerated microstructure of the HMW samples). This direct relationship between difference in lattice parameter and Tb content may be explained in three ways: it is mainly the Tb that is switching between +3 and +4 oxidation states; the presence of Tb facilitates the reduction and oxidation of the Ce; or it is a combination of both these effects. It is proposed that the first explanation is the correct one. There is much evidence showing that the reduced forms of terbium oxide, and Tb^{3+} in general, have greater stability than Ce^{3+} and reduced forms of cerium dioxide.[24,28-31] In addition, the XANES spectra taken under reducing conditions (presented in the next section, Table 5 and Figure 10) are in agreement with this in that they show that the Tb^{3+} content of these samples is high, and the Ce^{3+} content is significant but much lower. It is important to restate that lattice expansion under reducing conditions would be caused directly by the increase in ionic radius on going from Tb^{4+} to Tb^{3+} but also because of the accompanying formation of oxygen ion vacancies. The concentration of all three defects is controlled by the relationship given in Equation 1.

$$2\left|V_O^{\bullet\bullet}\right| = [Ce'_{Ce}] + [Tb'_{Ce}] \qquad (1)$$

This effect, whereby Tb^{3+} content increases while Ce^{3+} remains low, was previously shown by the authors for another multivalent rare earth.[18]

In situ XANES studies

The fractions of Ce present as Ce^{3+} ($Ce^{3+}/(Ce^{4+}+Ce^{3+})$) in the samples at 500ºC under reducing (5% H$_2$/He, 20 mL.min^{-1}) and oxidizing (synthetic air: 21% O$_2$/N$_2$, 50 ml.min^{-1}) conditions, were determined from the experimental XANES spectra (see Supporting Information, **Figures S5 a-h**) as previously described and are presented in **Table 5**. The negative values in **Table 5** simply indicate that the Ce^{3+} content of the TbDC samples is lower than in the reference material, pure, undoped CeO$_2$. If, as argued here, Tb^{3+} is more stable than Ce^{3+}, any reduction process induced by hydrogen treatment would be first experienced mostly by terbium, and only when terbium reduction to the +3 oxidation state was almost complete, would cerium start to be reduced to the +3 oxidation state.[24,28-31] Hence, these results should be taken as an indication of a very probable stabilization of Ce^{4+} due to Tb^{3+}.

All values were normalized to the fraction of Ce present as Ce^{3+} in pure CeO$_2$ at room temperature. The increase in the area of peak C in the spectra indicates that, at high temperature, the amount of Ce present as Ce^{3+} is larger under reducing conditions than under oxidizing conditions.

Table5. Fraction of Ce present as Ce^{3+} in TbDC10 and TbDC20 samples under reducing and oxidizing conditions at 500ºC, estimated from fittings to the Ce L_3-edge XANES spectra.

Sample	Atmosphere	$Ce^{3+}/(Ce^{4+}+Ce^{3+})$[a] (%)
TbDC10-HMW	5% H_2/He	4.8
	21% O_2/N_2	-1.5
TbDC20-HMW	5% H_2/He	1.8
	21% O_2/N_2	-2.9
TbDC10-CC	5% H_2/He	5.9
	21% O_2/N_2	-2.1
TbDC20-CC	5% H_2/He	7.1
	21% O_2/N_2	-4.9

[a] Values are calculated with respect to a standard material: pure, nanoparticulate ceria at room temperature. Negative values indicate that the sample contained a smaller percentage of Ce^{3+} than this standard.

Figure 10 a and **b** present the normalized XANES spectra at the Tb L_3-edge obtained at 500ºC under reducing (5% H_2/He, 20 mL.min^{-1}) and subsequent oxidizing (synthetic air: 21% O_2/N_2, 50 ml.min^{-1}) conditions, respectively, both for nanopowders (CC) and spheres (HMW). At first sight, it could be assumed that the extent of re-oxidation (seen as the Tb^{3+} switching to Tb^{4+} in oxidizing atmospheres) of these samples is rather low, since the white line assigned to Tb^{4+} is rather small.
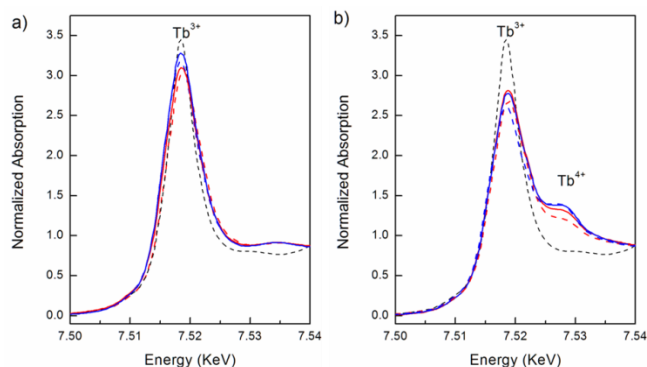

Figure 10. Normalized XANES spectra at the Tb L_3-edge obtained at 500ºC under (a) reducing and (b) subsequent oxidizing conditions for TbDC10-HMW (continuous red line), TbDC20-HMW (dotted red line), TbDC10-CC (continuous blue line) and TbDC20-CC (dotted blue line). Spectra for $Tb(NO_3)_3$ (Tb^{3+}; dotted black line) are included for comparison.

However, there are studies that show that even in XANES spectra of samples containing (nominally) 100% of the Tb in the +4 state, the white line for Tb^{4+} is not so pronounced, and that the presence of any peak should be taken as indicative of significant Tb^{4+} content.[32] Hence, our samples show significant levels of both Tb^{3+} and Tb^{4+} at 500ºC in oxidizing conditions. On the other hand, the spectra obtained under reducing conditions show that the terbium is completely reduced to Tb^{3+}. This is in agreement with the *in situ* SR-XRD results, where the moderate increase in lattice parameter can be ascribed to the increase in concentration of both Tb^{3+} and the related oxygen

vacancies. The reduction of Ce^{4+} also contributes to a lesser extent to this unit cell expansion. As the authors previously showed in a study of another multivalent rare earth,[18] Ce^{3+} content is not independent of Tb^{3+} content, but they are related to the maximum number of oxygen vacancies allowed for the structure. Results exhibited in **Table 5** indicate that Tb^{3+} cations stabilize Ce^{4+}. This argument is reinforced by the fact that an appreciable Tb^{3+} content is detected under oxidizing conditions at 500ºC and in air at room temperature.

Preliminary in situ EXAFS studies
Figure 11 shows the moduli of Fourier Transforms (FTs) of the EXAFS signal corresponding to the Tb L_3-edge for TbDC20 samples synthesized by CC and HMW methods and recorded at room temperature, at 500ºC in 5% H_2/He and at 500ºC in air. The calculated FT of the theoretical EXAFS signal of a fluorite-like structure with 10 mol% Tb replacing Ce in the 2a site of the Fm-3m space group is also included in Figure 11 b. This calculation was performed using the Feff8.20 program. The calculated FT function was multiplied by a factor of 0.2 in order to make the peak's heights fit those of the experimental plot.
The first peak, located between R=1.6 and 2.2 Å, is ascribable to the oxygen nearest neighbors (NN, or first O shell). The second peak, between R=3 and 4 Å, contains information about the second shell (Tb and Ce) and the third shell (O). Peaks located at R<1.5 Å correspond to smooth background oscillations in the absorption spectrum that have no relation to the EXAFS processes.
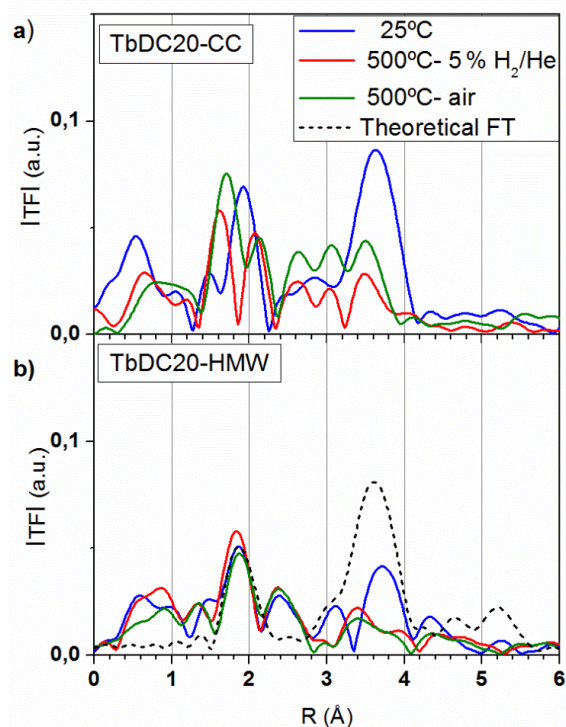

Figure 11. Fourier Transforms (FTs) of the EXAFS signal corresponding to the Tb L_3-edge for TbDC20 samples synthesized by CC (a) and HMW (b) methods at room temperature (blue line), at 500ºC in 5% H_2/He (red line) and at 500ºC in air

(green line). The calculated FT of the theoretical EXAFS signal of a fluorite-like structure is included (black dotted line) for comparison.

The difference in height between the calculated and experimental FTs may be due to thermal and structural disorder in the samples and also to differences between the expected (calculated) and experimental local order. In particular, in a fluorite-like structure, Tb is expected to have eight oxygen NNs. However, as XANES analyses showed the existence of a majority of Tb in the +3 oxidation state, the resulting presence of oxygen vacancies would be expected to decrease the number of NNs and so the FT would show a smaller first peak.

In addition, as roughly 30% of unit cells in nanopowders with crystallites of 10 nm diameter are on the crystallite's surface, more than 10% of Tb will have coordination numbers of about half the expected value (typically, 8 oxygens, 12 cations and 24 oxygen anions, for the first, second and third shells, respectively). This crystallite size effect would contribute to make the peaks in the FT function smaller than those predicted by calculation, as shown in **Figure 11**. At room temperature, FT of TbDC20-CC (**Figure 11a**, blue line) has the second peak higher than the first one, in accordance with the theoretical FT. However, at 500ºC this relationship is inverted.

This is principally ascribable to an increased thermal disorder and possibly a change in the local order related to the second and third shells. Comparing the FTs for TbDC20-CC at 500ºC under reducing and oxidizing conditions, the higher peaks in the latter may be an indication of re-filled oxygen sites. This is in agreement with the XANES analyses which showed that Tb in samples under reducing conditions is almost all in the +3 oxidation state and after switching to oxidizing conditions a large fraction of Tb^{3+} changes to Tb^{4+} (**Figure 10b**). The peaks in the FTs of TbDC20-HMW in Figure 11b are all smaller than, and of different shape to, those of TbDC20-CC. This may be due to greater disorder or to different local order around the Tb atom in the TbDC20-HMW sample. The inverted height relationship between the first and second peaks (observed at 500ºC in TbDC20-CC) is also present here, even at room temperature. This suggests that this feature is more likely related to structural disorder or changes in the local order than to thermal disorder. Moreover, the shape and height of the first peak remain essentially unaltered. On the other hand, it seems that thermal disorder does influence the changes observed in the second peak on going from room temperature to 500ºC, although the change in its shape suggests a different local order at high temperature also. The evolution of the first peak for TbDC20-HMW with the environmental conditions recalls the changes in the corresponding XANES results (**Figures 8b** and **10a** and **b**), where no major differences were observed between spectra obtained at room temperature and at 500ºC in synthetic air.

A detailed study of the local order of Tb in TbDC samples is currently being performed in which different models of local order are analyzed. Moreover, theoretical calculations using ab initio density functional theory (DFT+U) will be performed in order to support the different models. Of special interest is the question of whether the presence of vacancies is predicted under the environmental conditions employed for this study and, if so, where they are located and where the oxygen atoms are located. This is a very important issue since oxygen vacancies play a central role in the transport properties of these materials.

Figure 12 a and **b**, shows FTs of EXAFS spectra corresponding to the Ce L3-edge for TbDC20 synthesized by CC and HMW methods, and recorded first in air at room

temperature (blue line), then in 5%H_2/He at 500ºC (red line) and finally in synthetic air at 500ºC (green line). For comparison, the theoretical FT corresponding to CeO_2 with the Fm-3m space group (dashed line) and the experimental FT of CeO_2 synthesized by the HMW method (black line) are also included. The theoretical FT was multiplied by a factor of 0.5 in order to make the peak heights fit better with those of the experimental plots.

As explained in the case of the Tb L_3-edge analysis, the difference in height between the theoretical and the experimental FTs can be ascribed to structural disorder in the experimental samples. The inversion in the relationship of the heights of the first and second peaks between experimental and theoretical FTs, on the other hand, may be due to the crystallite size effect, (~10 nm). As mentioned above, at this scale, surface effects are important and may yield a lower average coordination number for the second and more distant shells, as well as an increase of structural disorder.
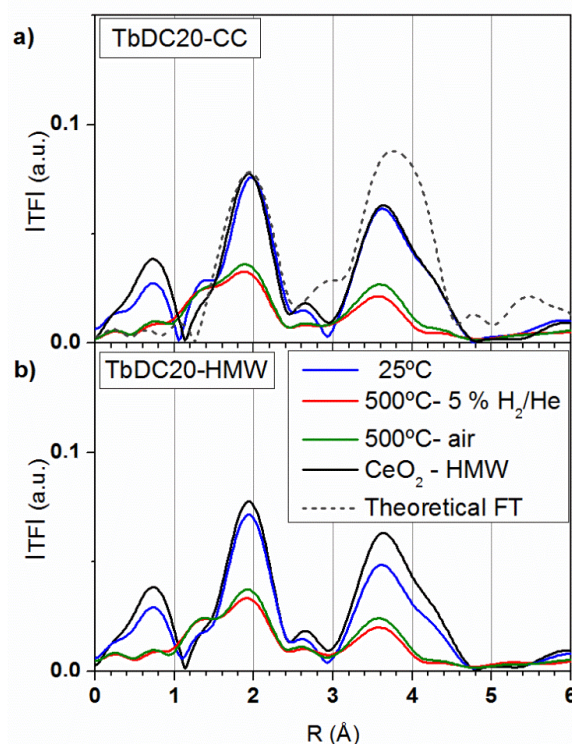

Figure 12. Fourier Transforms (FTs) of the EXAFS signal corresponding to the Ce L_3-edge for TbDC20 synthesized by CC (a) and HMW (b) and recorded in air at room temperature (blue line) and in 5%H_2/He (red line) and in synthetic air (green line), both at 500ºC. For comparison, the theoretical FTs for CeO_2 with Fm-3m space group (dashed line) and the experimental FTs of CeO_2 synthesized by the HMW method (black line) are also included.

Only negligible differences exist at room temperature between the FTs of the TbDC20-CC and the CeO_2 reference sample, which suggests that there are very few oxygen vacancies in the local environment of Ce in TbDC20-CC (in accordance with XANES results for the Ce L_3-edge) and that there are no perceptible distortions in the cation lattice that may further affect Ce-cation distance or the coordination numbers of the

second and third shells. On heating to 500ºC, the marked decrease in the height of the peaks can be ascribed to thermal disorder, since the XANES analyses showed that almost all the Ce is in the +4 oxidation state under oxidizing conditions. On the other hand, a small number of oxygen vacancies seem to be generated under reducing conditions, giving rise to a further decrease in peak height in the FT, which is also in accordance with the XANES analyses.

The FTs for TbDC20-HMW showed apparent differences with respect to the CeO_2-HMW sample at room temperature (and also with respect to the TbDC20-CC nanopowder), while at 500ºC the behavior was essentially the same as that of TbDC20-CC (**Figure 12 b**). At room temperature the peaks for TbDC20-HMW are smaller than for TbDC20-CC. The XANES Ce L_3-edge results showed no significant difference in Ce^{3+} content between these two samples. Therefore, this difference may be an indication that there was greater structural disorder in the nanospheres. This was also suggested by the EXAFS results for Tb (**Figure 11**).

Structural models that correctly fitted the experimental local orders around Ce and Tb differed significantly from that expected for cations in a fluorite-like structure. DFT+U calculations will be needed to validate these models.

Conclusions

In the present work, $Ce_{1-x}Tb_xO_{2-\delta}$ (x = 0.1 and 0.2) solid solutions with different nanoscale morphologies were synthesized by cation complexation and microwave assisted hydrothermal homogeneous co-precipitation, to give nanopowders and spheres, respectively. All samples were composed of nanocrystallites with a size of around 10 nm. The samples prepared by HMW exhibited values of specific surface area of 28 and 18 $m^2.g^{-1}$ for TbDC10 and TbDC20, respectively.

Electron microscopy images confirmed the formation in very high yield of particles of uniform spherical morphology and narrow size distribution by the HMW method. The spheres were about 200 nm across and slightly larger for the sample with the higher Tb content. In TEM they were seen to consist of many tightly-packed crystallites of around 10 nm in size. EDS confirmed their chemical compositions to be close to the target values and elemental maps of small clusters of spheres indicated that their chemical compositions were homogeneous.

In situ XRD experiments showed an increase in lattice parameter on reduction which was attributed to the reduction of Ce^{4+} and Tb^{4+} cations to Ce^{3+} and Tb^{3+}, which have larger radii, and to the associated increase in V_O concentration.

XANES experiments at the Ce and Tb L_3-edges showed that the changes observed on reduction of the Tb-containing samples resulted mostly from the formation of Tb^{3+} rather than Ce^{3+}, and supported the previously-reported proposal that Tb^{3+} acts to stabilize Ce^{4+} to some extent.

Preliminary EXAFS studies at the Ce and Tb L_3-edges showed that the changes observed in the oxidation state of the Tb has an important influence on the local order of both cations but that these were more pronounced for Tb than Ce. The EXAFS analyses suggest the existence of qualitative differences in the local order around Tb between the nanopowders and nanospheres. This is the case both at room temperature and at high temperature when switching from reducing to oxidizing conditions. In addition, it is apparent that there is greater structural disorder in the nanostructured spheres than in the nanopowders. In all cases, the cation's local order seemed to be qualitatively different from that expected for a fluorite-like structure.

Notes and references

[a] CINSO (Centro de Investigaciones en Sólidos), CONICET-CITEDEF, J.B. de La Salle 4397, 1603 Villa Martelli, Buenos Aires, Argentina.

[b] CONICET, Buenos Aires, Argentina.

[c] Departamento de Física, Centro Atómico Constituyentes, CNEA, Av. Gral. Paz 1499, (1650) San Martín, Buenos Aires, Argentina.

[d] Escuela de Ciencia y Tecnología, Universidad Nacional de San Martín, M.de Yrigoyen 3100 (1650) San Martín, Buenos Aires, Argentina.

[e] EaStChem, School of Chemistry, University of St. Andrews, North Haugh, St. Andrews, Fife, KY16 9ST, United Kingdom.

1   R. Di Monte, Kaspar, *J. Top. Catal.* 2004, **28**, 47-57.

2   S. D. Park, J. M. Vohs, R. J. Gorte, *Nature* 2000, **404**, 265-267.

3   Haile, S. M. Mater. Today 2003, **6**, 24-29.

4   T. Kim, J. M. Vohs, R. J. Gorte, *Ind. Eng. Chem. Res.* 2006, **45**, 5561-5565.

5   R. J. Gorte, *AIChE Journal* 2010, **56**, 1126-1135.

6   J. A. Kilner, *Solid State Ionics* 2000, **123**, 13-23.

7   B. C. H. Steele, *Solid State Ionics* 2000, **129**, 95-110.

8   B. Dalset, P. Blennov, P. Van Hendriksen, N. Bonannos, D. Lybye M. Mogensen, *J. Solid State Electrochem.* 2006, **10**, 547-561.

9   R. O. Fuentes, R. T. Baker, *Int. J. Hydrogen Energy* 2008, **33**, 3080-3084

10 V. V. Kharton, F. M. Figueiredo, L. Navarro, E. N. Naumovich, A. V. Kovalevsky, A. A. Yaremchenko, A. P. Viskup, A. Carneiro, F. M. B. Marques, J. R. Frade, *J. Mater. Sci.* 2001, 36 5, 1105–1117.

11 R. O. Fuentes, F. F. Muñoz, L. M. Acuña, A. G. Leyva, R. T. Baker, *J. Mater. Chem.* 2008, **18**, 5689-5795.

12 M. Balaguer, C. Solís, J. M. Serra, *J. Phys. Chem. C* 2012, **116** 7975-7982.

13 D. P. Fagg, A. L. Shaula, V. V. Kharton, J. R. Frade, *J. Membr. Sci.* 2007, **299**, 1–7.

14 M. Balaguer, C. Solís, S. Roitsch, J. M. Serra, *Dalton Trans.* 2014, **43**, 4305-4312.

15 M. Balaguer, C-Y Yoo, H. J. M. Bouwmeester, J. M. Serra, *J. Mater. Chem. A* 2013, **1**, 10234-10242.

16 A. B. Hungría, A. Martínez-Arias, M. Fernández-García, A. Iglesias-Juez, A. Guerrero-Ruiz, J. J. Calvino, J. C. Conesa, J. Soria, *Chem. Mater.* 2003, **15**, 4309-4316.

17 X. Wang, J. C. Hanson, G. Liu, J. A. Rodríguez, A. Iglesias-Juez, M. J. Fernández-García, *Chem. Phys.* 2004, **121** 11, 5434-5444.

18 F. F. Muñoz, L. M. Acuña, C. Albornoz, A. G. Leyva, R. T. Baker, R. O. Fuentes, *Nanoscale,* 2015, **7**, 271-281.

[19] H. Klug, L. Alexander in: *X-ray Diffraction Procedures for Polycrystalline and Amorphous Materials*, John Wiley, New York, 1974, p. 618.

20 J. Rodríguez-Carvajal, FullProf Suite Program, Version 2.05. Laboratoire León Brillouin. Saclay, France: CEA-CNRS; 2011.

21 R. A. Young, in: R. A. Young (Ed) *The Rietveld Method*, Oxford University Press, Oxford, 1993, Chapter 1, pp. 21-24.

22 G. Adachi, Z. C. Kang, in: G. Adachi, N. Imanaka, Z. C. Kang (Eds), *Binary Rare Earth Oxides*, Kluwer Academic Publishers, Dordrecht, 2004, 2-3.

23 E. Schweda, Z. C. Kang, in: G. Adachi, N. Imanaka, Z. C. Kang (Eds), *Binary Rare Earth Oxides*, Kluwer Academic Publishers, Dordrecht, 2004, 90.

24 S. Bernal, G. Blanco, J. M. Gatica, J. A. Perez Omil, J. M. Pintado, H. Vidal in: G. Adachi, N. Imanaka, Z.C. Kang (Eds), *Binary Rare Earth Oxides*, Kluwer Academic Publishers, Dordrecht, 2004, 32-34.

25 S. Bernal, G. Blanco, J. J. Calvino, J. A. Pérez Omil, J. M. Pintado. *Journal of Alloys and Compounds* 2006, **408-412**, 496–502.

26 F. Zhang, P. Wang, J. Koberstein, S. Khalid, S. W. Chan, *Surf. Sci.* 2004, **563**, 74-82.

27 F. F. Muñoz, R. T. Baker, A. G. Leyva, R. O. Fuentes, *Appl. Catal. B: Environmental* 2013, **136-137**, 122-132.

28 S. Bernal, G. Blanco, J. M. Pintado, J. M. Rodríguez-Izquierdo, M. P. Yeste, *Catalysis Communications* 2005, **6**, 582–585.

28 A. Martínez-Arias, A. B. Hungría, M. Fernández-García, A. Iglesias-Juez, J. C. Conesa, G. C. Mather, G. Munuera, *Journal of Power Sources* 2005, **151**, 43–51.

30 S. Colussi, C. de Leitenburg, G. Dolcetti, A. Trovarelli, *Journal of Alloys and Compounds* 2004, **374**, 387–392.

31 X. Wang, J. C. Hanson, G. Liu, J. A. Rodríguez, *J. Chem. Phys.*, 2004, 121, 5434.

32 I. A. Sluchinskaya, A. I. Lebedev, A. Erko, *Physics of the Solid State* 2012, **54** 5, 975–979.